Lab on a Chip

PAPER

View Article Online
View Journal | View Issue

Cite this: *Lab Chip*, 2019, **19**, 1267

Intensity-modulated nanoplasmonic interferometric sensor for MMP-9 detection†

Yifeng Qian, [a] Xie Zeng, [a] Yongkang Gao, [b] Hang Li, [c] Sushil Kumar, [a] Qiaoqiang Gan, [d] Xuanhong Cheng *[c] and Filbert J. Bartoli*[a]

Received 20th December 2018,
Accepted 21st February 2019

DOI: 10.1039/c8lc01391h

rsc.li/loc

To elucidate the secretary function of immune cells, we develop a nanoplasmonic circular interferometric biosensor based on intensity interrogation for label-free and dynamic sensing of molecular secretion. Exceptional sensitivity has been demonstrated through coupling free light and surface plasmon polariton (SPPs) waves, which generates a constructive and deconstructive interference pattern with high contrast and narrow linewidth when illuminated by white light. Alternatively, by adopting a narrow-band LED source and a CCD camera in this work, the transmission intensity of multiple sensing units is monitored simultaneously with a simple collinear optical setup. This intensity-modulated sensing platform yields a resolution of 4.1×10^{-5} refractive index unit (RIU) with a high temporal resolution of 1 s and a miniaturized footprint as small as $9.8 \times 9.8\ \mu m^2$ for a single sensing unit. By integrating the signals from multiple sensor units, the resolution of a 12×12 sensor array was found to reach 7.3×10^{-6} RIU. We apply this sensor array to detect matrix metalloproteinase 9 (MMP-9) secretion from human monocytic cells, THP-1, at different time points after lipopolysaccharide (LPS) simulation and the results are in good agreement with enzyme-linked immunosorbent assay (ELISA) tests, but without the need for labeling. The spatial, temporal and mass resolutions of the sensor array are found to exceed other label-free technologies. These biomolecular arrays, incorporated in a microfluidic sensor platform, hold great potential for the study the dynamics and interplay of cell secretion signals and achieving a better understanding of single cell functions.

Introduction

Biosensors based on the surface plasmon resonance (SPR) principle have been widely adopted for quantifying biomolecule interactions in real-time and in a label-free fashion.[1] Surface plasmons (SPs) are electromagnetically excited coherent charge oscillations highly confined at a metal-dielectric interface.[2] The tightly confined optical field is very sensitive to the local surface refractive index change, making SPR suitable for detecting biomolecule binding on a substrate.[3] Among the various approaches reported, conventional SPR sensors based on the Kretschmann configuration[4] are the most popular and can achieve a limit of detection of 10^{-6}–10^{-7} refractive index units (RIU).[5] However, the prism-based setup and oblique angle of incidence make it difficult to align and miniaturize. Another significant limitation of SPR spectroscopy is the challenge of multiplexing[6,7] due to the poor time and spatial resolution of spectrometers used to detect the reflected light at different wavelengths.[5] To achieve high-throughput and label-free biosensing, SPR imaging/microscopy (SPRi/SPRM) has been proposed[8] and has drawn increasing attention in the past two decades in drug discovery, diagnostics, biomolecular detection and food safety applications.[9] In a typical SPRi/SPRM setup, the spectrometer used in the Kretschmann configuration is replaced by a CCD camera to detect the intensity of reflected light from different regions on the sensor surface. While SPRi/SPRM typically has a high detection resolution of $\sim 2 \times 10^{-5}$–5×10^{-6} RIU,[10,11] the prism configuration is bulky and difficult to miniaturize or scale up, since the oblique reflection angle and tilted image plane result in optical aberration and difficulty in focusing.[12,13] Moreover, the prism-based setup prevents usage of optics with high numerical apertures (NA), limiting spatial resolution and the corresponding density of the sensing spots.[12,14,15] Typically, SPRi systems use sensing spots of 200–300 μm in diameter or larger[10,11,16,17] in order to obtain a desirable signal-to-noise ratio.

Nanoplasmonic sensors employing nanoparticles,[18] nanopatterned gratings,[19] or hole arrays[20] on metallic films overcome the aforementioned shortcomings of conventional SPR

[a] *Electrical and Computer Engineering Department, Lehigh University, Bethlehem, PA, 18015, USA. E-mail: fjb205@lehigh.edu*
[b] *NeoPhotonics, San Jose, CA, 95134, USA*
[c] *Materials Science and Engineering Department, Bioengineering Department, Lehigh University, Bethlehem, PA, 18015, USA. E-mail: xuc207@lehigh.edu*
[d] *Electrical Engineering Department, University at Buffalo, The State University of New York, Buffalo, NY, 14150, USA*

† Electronic supplementary information (ESI) available. See DOI: 10.1039/c8lc01391h

systems and have attracted increasing interest in recent years.[21] In these sensors, incident light is directly coupled through the localized surface plasmon resonance (LSPR) or SPPs and the resonance frequency is very sensitive to local refractive index. These nanoplasmonic sensors can have a footprint as small as a few micrometers,[22,23] permitting high density sensor arrays for massive multiplexing.[24] Among nanostructured plasmonic sensors, nanohole arrays exhibiting extraordinary optical transmission (EOT)[25] have emerged in recent years as a popular option for biomarker diagnostic applications.[26] Similar to conventional SPRi, a typical nanoplasmonic imager combines a CCD camera and narrow-bandwidth light source, but with an upright microscope instead of slanted light source and detector. Consequently, the CCD camera detects collinear light transmission instead of reflected light, facilitating alignment and allowing the use of high-NA optics to improve the signal-to-noise ratio in intensity-based detection. However, the sensing performance of most reported platforms suffers from broad linewidth due to strong radiative damping and dissipation losses of LSPRs.[27]

In this work, we develop a new nanoplasmonic interferometer imaging system for sensitive and label-free detection of biomolecules. The sensor contains an array of hole-ring interferometers[28] and each unit has a footprint as small as 9.8 × 9.8 μm^2. The intensity-modulated imaging platform uses an LED-filter combination as the illumination source and a CCD camera as the detector. The intensity of transmitted light through multiple sensing units is recorded simultaneously on the CCD camera. The performance of the sensor array was first calibrated and the refractive index resolution determined by varying the bulk refractive index. The optimal signal integration scheme was then used to study dynamic MMP-9 secretion from THP-1 cells in the cell culture supernatant and results were compared against conventional biochemical assays. The potential of this biosensor for multiplexed biomolecule sensing is discussed at the end of the paper.

Cell secretion of chemokines, cytokines and proteases plays a significant role in various physiological and pathological processes, and understanding the secretion behaviour is critical in many biomedical fields.[29] In particular, the secretion of MMPs has been studied due to the important roles it plays in organogenesis, normal tissue turnover, inflammation, tumor development and infection.[30–33] Biochemical assays of MMP concentration by ELISA, although sensitive, are tedious and time consuming.[34] The label-free approach presented here improves the analysis speed and could potentially be integrated with live cell/tissue culture for *in situ* MMP-9 detection. The imaging capability of the reported sensor array also offers the opportunity for multiplexed sensing of different secretory molecules to understand their interplay in cell function.

Materials and methods

Chemicals and biomolecules

Glycerol was purchased from Alfa Aesar. 11-Mercaptoundecanoic acid (MUA) was purchased from Santa Cruz Biotechnology. *N*-(3-Dimethylaminopropyl)-*N*′-ethylcarbodiimide (EDC), *N*-hydroxysuccinimide (NHS), 2-(*N*-morpholino)ethanesulfonic acid (MES), phosphate buffered saline 10× (PBS 10×), glutaraldehyde (G6257), casein (C7078) and lipopolysaccharides (LPS) (L4391) were purchased from Sigma-Aldrich. Anti-MMP-9 (Clone M2108F07, Lot P23711), MMP-9 (Cat 550504, Lot B198085) and human MMP-9 ELISA kit (Lot B232170) were purchased from BioLegend. THP-1 (TIB-202) cells were purchased from ATCC. RPMI-1640 medium (Lot 1868989) and 2-mercaptoethanol (Cat 21985023) were purchased from Gibco. Fetal bovine serum was purchased from Invitrogen. Penicillin and streptomycin were purchased from Gibco.

Fabrication of nanoplasmonic interferometer sensors

Films of 5 nm thick titanium and 250 nm thick gold were deposited consecutively onto a precleaned glass microscope slide (Fisher Scientific) *via* E-beam evaporation (Indel system). The deposition rate was 0.1 nm s^{-1}. The root mean square roughness is 2.1 nm (Fig. S1†), measured by NT-MDT Solver NEXT AFM. Afterwards, a focused ion beam of 30 kV and 50 pA (FIB, FEI Scios DualBeam) was used to mill a 12 × 12 array of circular ring-hole interferometers. The center-to-center distance between neighboring sensors is 12.5 μm in both in *x*- and *y*-directions. Oxygen plasma treatment (March Instruments PX250) was used to clean the sensor surface after milling of the structure by FIB.

Microfluidic channel fabrication and device assembly

Microfluidic channels were fabricated by standard soft lithography. Briefly, SU-8 (MicroChem) was patterned on a 3 inch silicon wafer with designed structures. Afterwards, a 10 : 1 ratio of polydimethylsiloxane (PDMS, Dow Corning) and curing agent (Dow Corning) was mixed and poured onto the silicon mold. After baking for 5 hours at 70 °C, PDMS was peeled off and inlet and outlet holes were created. The microfluidic channel chamber has a cross-sectional area of 14 × 4 mm^2 and a height of 50 μm. Finally, the microfluidic channel was integrated with the sensor chip using a custom designed manifold.

Optical measurements

An inverted microscope (Olympus IX81) was used to detect transmitted light through the sensor chip. For spectral measurements, a halogen lamp was used as the light source. Transmitted light was collected by a 40× objective lens (NA = 0.6) and coupled to a portable fiber-optic spectrometer (Ocean Optics, QE65Pro). For intensity modulation, a red LED (Thorlabs, M660L4), controlled by an LED driver (Thorlabs, DC2200), was combined with a filter (Semrock) with peak wavelength of ~661 nm and full width of half maximum (FWHM) of 15.9 nm. A CCD camera (Cooke SensiCam QE) was used for intensity acquisition.

Bulk sensing experiments

To calibrate the sensitivity of the nanoplasmonic interferometer array, glycerol–water mixtures, with concentrations ranging from 0% to 10%, were injected into the channel at 15 μL min^{-1} using a syringe pump (Chemyx, fusion 200). The sensor array was illuminated by the LED in pulse mode with a 20% duty cycle. The transmitted intensity was imaged by the CCD camera with an exposure time of 250 ms. Every four images were averaged by the microscope controlling software (Slidebook) before storage.

Biosensor surface modification

To immobilize antibodies on the sensor surface, the bare sensor chips were incubated with 11-mercaptoundecanoic acid (MUA) at a concentration of 10 mM in 200 proof ethanol for 10 hours to form a self-assembled monolayer. After rinsing the surfaces three times in ethanol, the devices were incubated with a mixture of 400 mM of EDC and 100 mM of NHS in MES buffer for 30 minutes to activate the carboxyl groups in MUA. Then the sensor chip was integrated with the microfluidic channel using a custom designed manifold. A solution of 20 μg mL^{-1} anti-MMP-9 was passed through the channels at 15 μL min^{-1} for 30 minutes. Afterwards, 0.05% glutaraldehyde and 1 mg mL^{-1} casein were introduced at a flow rate of 5 μL min^{-1} for 1 hour and 2 hours, respectively, to fix the antibody and reduce non-specific binding.

Cell culture and stimulation

The THP-1 cells were cultured in RPMI-1640 medium supplemented with 0.05 mM 2-mercaptoethanol, 10% fetal bovine serum, 100 units per mL penicillin and 100 μg mL^{-1} streptomycin at 37 °C and 5% CO_2. The cells were subcultured by adding fresh medium twice a week. To study the time evolution of MMP-9 secretion, THP-1 cells were cultured in 12-well low adhesion plates (Corning) until the cell number in each 1 mL well reached 0.8 million, which is the subculture concentration recommended by ATCC. Next, lipopolysaccharide (LPS) was added to each well at a final concentration of 10 μg mL^{-1} to stimulate MMP-9 secretion. The supernatant was collected hourly from separate wells up to 12 hours, centrifuged to remove the cell debris and stored frozen at −80 °C until testing.

Calibration and detection of MMP-9 binding

The calibration curve for MMP-9 detection was obtained by injecting various concentrations (0, 50, 100, 150, 200 ng mL^{-1}) of MMP-9 in THP-1 culture medium into freshly functionalized microfluidic channels at a flow rate of 5 μL min^{-1} for 1.5 hour. For the detection of MMP-9 from cell culture samples, the collected supernatant samples at selected time points were continuously passed across the sensor surface at 5 μL min^{-1} for 1.5 hour. Intensity images were acquired as described above. To confirm these label-free sensing measurements, the MMP-9 concentration in the supernatant was further analyzed using an ELISA kit following a protocol suggested by the manufacturer.

Data analysis

A linear regression was applied in data fitting for bulk sensing and the MMP-9 calibration. In all tests, at least three samples were measured and mean and standard deviations are shown in the figures unless otherwise noted.

Principle of operation of the circular interferometer

As shown in Fig. 1a and b, a single plasmonic interferometer sensor consists of three concentric nanogrooves milled in a 250 nm thick gold film along with a single nanoaperture in the center of the structure. When the normally incident light impinges on the nanostructured surface, SPPs are generated in the grooves and propagate along the radial direction to the central nanohole,[35] where they interfere with light directly transmitted through the central hole. The theoretical transmission intensity can be expressed as:

$$I = I_{\text{free}} + I_{\text{spp}} + 2\sqrt{I_{\text{free}} I_{\text{spp}}}\cos\left(k_{\text{sp}} R + \varphi_0\right) \quad (1)$$

where I_{free} and I_{spp} denote the light intensity transmitted directly through the central hole and that mediated by SPPs, respectively; $k_{\text{sp}} = \left(\frac{2\pi}{\lambda}\right)\sqrt{\frac{\varepsilon_{\text{m}}\varepsilon_{\text{d}}}{\varepsilon_{\text{m}} + \varepsilon_{\text{d}}}}$ represents the propagation constant of SPPs, in which λ is the incident wavelength, and ε_{m} and ε_{d} are the permittivity of gold and the dielectric medium covering the sensor surface, respectively; R is the radius of the middle groove and φ_0 is an intrinsic phase shift associated with SPP excitation at the grooves.[36] The term $(k_{\text{sp}}R + \varphi_0)$ denotes the phase difference between the two interfering components. Under broadband illumination, the transmission spectrum is modulated sinusoidally, exhibiting constructive and destructive interference as $k_{\text{sp}}(\lambda, \varepsilon_{\text{d}})$ varies. Fig. 1c shows typical transmission interference spectra under white light illumination, for the cases when the surface is exposed to water (black curve) and to a 10% water–glycerol mixture (black dashed curve). With increasing ε_{d}, the interference pattern exhibits an obvious red-shift (see black dashed curve), which has been monitored in our prior work for spectral biosensing.[28] At the same time, the shift of the interference pattern leads to changes of transmitted intensity at a fixed wavelength. Grey/blue shaded areas in Fig. 1c denote the wavelength ranges within which the transmitted intensity changes either positively or negatively corresponding to increasing refractive index change on the sensor surface.

Since spectral interrogation is not suitable for imaging purposes, we employ intensity interrogation, where a red LED light is employed for illumination and a CCD camera is used

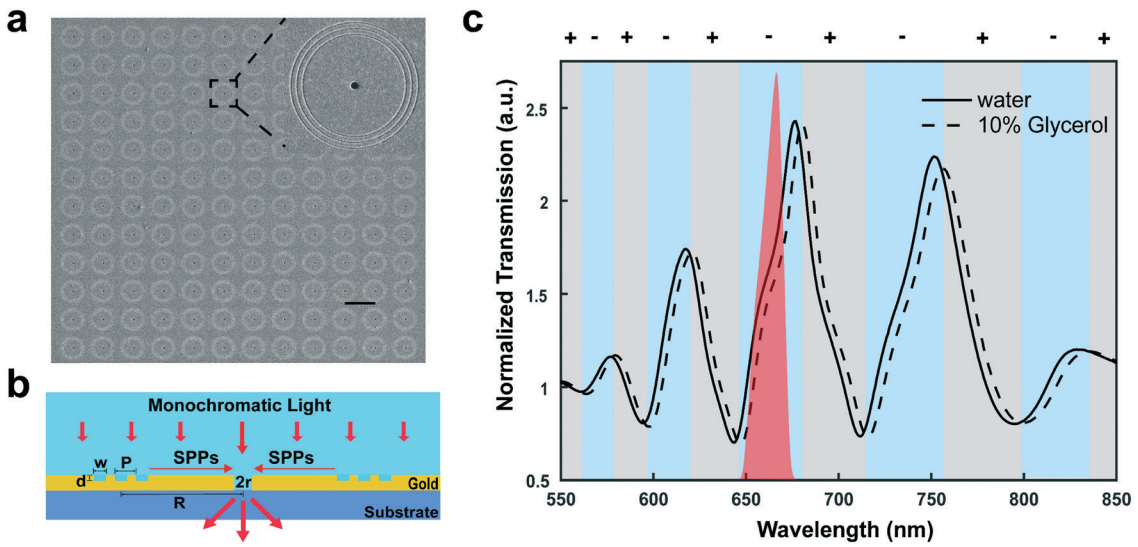

Fig. 1 The principle of operation of a single circular plasmonic interferometer. (a) A SEM image of the 12 × 12 interferometer array. Scale bar = 12.5 μm. Inset is a magnified SEM image of a single interferometer showing the ring-hole structure. (b) Side view of the nanoplasmonic device and propagation of two interfering components. (c) Transmission interference spectra under white light illumination when the surface is exposed to water (black line) and 10% water–glycerol (black dashed line) mixture. The grey/blue shaded areas denote the range of wavelength within which the intensity change is positive (+) or negative (–) with exposure to 10% glycerol compared to water. The red shaded area denotes the spectral line shape of a red LED used as the illumination source.

to simultaneously detect the intensity variation of transmitted light from an array of nanoplasmonic interferometers. A band-pass filter is used to further narrow the spectral line shape of the illumination light, illustrated by the red shaded area in Fig. 1c.

In our design, several parameters were tuned to optimize the sensor performance in intensity-interrogation mode. The groove periodicity (P = 470 nm), groove width (w = 220 nm) and groove depth (d = 50 nm) were varied carefully to maximize I_{spp} at the peak illumination wavelength ($\lambda \approx 661$ nm) in a water environment. The radius of the central nanohole (r) was set to 300 nm to balance I_{free} with I_{spp} in order to achieve the highest interference contrast. R was selected as ~4.3 μm considering the tradeoffs in sensor sensitivity, noise, footprint and dynamical range of detection. Larger R leads to a narrower interference linewidth[37] and hence enhances the sensor sensitivity. However, interference linewidth has to be broad enough to ensure that the illumination spectrum is positioned between the interference peak at $\lambda_p \approx 677$ nm and its neighboring interference valley at $\lambda_v \approx 643$ nm over the whole dynamic range of detection. In this way, the variation of the transmitted intensity is similar for all illumination wavelengths (decreasing in response to increasing surface refractive index), and also varies monotonically within the defined dynamic range of surface refractive index change. In addition, if R is too large, the SP propagation loss increases and degrades the signal-to-noise ratio. The increased sensor footprint would also limit the packing density and spatial resolution.

From eqn (1), we derived a relation between R and interference peak wavelength λ_p, assuming ε_m, ε_d and φ_0 to be constant,[28]

$$\frac{\Delta\lambda_p}{\Delta R} = \frac{\lambda_p}{R} = \text{constant} \quad (2)$$

Eqn (2) is a theoretical guideline for us to further adjust the interference peak wavelength λ_p relative to the position of LED illumination spectrum. Our strategy was to tune the initial λ_p to be slightly larger than the incidental peak wavelength to achieve optimal overlap between the sensor interference spectrum and illumination spectrum, *i.e.* the light intensity of sensor output achieved a maximum in a baseline environment and decreases as the refractive index of the sensor surface increases over the whole dynamic range of detection. The detector exposure time was also adjusted in the baseline environment to nearly saturate the CCD pixels in order to obtain the best signal-to-noise ratio. The sensor response is defined as the relative change of light intensity, $\frac{I - I_0}{I_0} \times 100\%$, where I_0 and I represent the transmitted intensity in the baseline and test environment, respectively.

Results and discussion

Interferometer array fabrication and refractometric characterization

Following the design of the circular interferometer, FIB milling was applied to fabricate the plasmonic sensor. A 250 nm thick gold film was deposited following a 5 nm titanium adhesion layer by electron-beam evaporation onto a glass substrate. A 12 × 12 array of ring-hole interferometers was milled by FIB in the deposited gold film, and the resulting scanning electron microscope (SEM) image is shown in Fig. 1a. The

pitch of 12.5 μm in both *x*- and *y*-directions was selected to avoid crosstalk[15] between neighboring sensors. A magnified SEM image of a single sensor element is shown as the inset in Fig. 1a.

The sensor was then integrated with a polydimethylsiloxane (PDMS) microfluidic channel and exposed to glycerol–water mixtures of various concentrations ranging from 0–10% glycerol, corresponding to bulk refractive indices of 1.3328 to 1.3444. This range covers that of THP1 culture medium, which is essential for sensing of cell secretion as the target biomolecule MMP-9 is secreted by stimulating THP-1 cells in the culture medium.[34] The device was placed on an inverted microscope and illuminated by narrow-band LED light, whose center wavelength is ~661 nm with a FWHM of 15.9 nm. Light transmitted through 12 × 12 sensing spots was simultaneously collected by a 40× object (NA = 0.6) and coupled by a lens into a CCD camera as illustrated in Fig. 2a, permitting real-time imaging of the entire sensor array. The sensor was imaged with an exposure time of 250 ms and every 4 images were averaged to improve the signal to noise ratio, resulting in a temporal resolution of one image per second. The intensity signals of individual sensors reveal the local refractive index changes and the array generates an intensity map. Unlike wavelength modulation where intensity changes are integrated over a broad range of wavelengths, the intensity-interrogation mode monitors changes within a narrowband wavelength range using an LED as the illumination source. The dynamic response of individual sensors is defined as the relative intensity change normalized to the initial transmission: $\mathrm{IR} = \left(\frac{I - I_0}{I_0}\right) \times 100\%$, where I and I_0 are the transmitted intensity at time t and t_0 respectively. The transmitted intensity I is obtained by integrating intensity from 11 × 11 pixels around the central pixel in each sensing unit. A zoomed-in optical image of a single senor is shown as the inset in Fig. 2b. The center of the sensor is identified as the pixel with the highest intensity (marked as the red dashed square). The relative intensity of the neighboring 7 pixels on each side in the horizontal direction is shown in Fig. 2c. The intensity decreases gradually and down to below 10% 5–6 pixels away from the center. To increase the signal-to-noise ratio, only 11 × 11 pixels (shaded areas) with appreciable intensity are integrated as the intensity of a single sensor. A background image without light illumination is collected and intensity integrated over the same area is subtracted from the signal images. Fig. 3a shows the integrated response of the 12 × 12 interferometer array in response to bulk refractive index changes. As shown in the inset, the noise level of the sensor array is found to be 0.015%, calculated over a 2 minute span (120 points). Fig. 3b shows the interferometer response as a function of refractive index change. The linear fit reveals a sensitivity $\left(S = \left|\frac{\Delta \mathrm{IR}}{\Delta \mathrm{RI}}\right|\right)$ of 2.05 × 10^3% per RIU and the intercept was forced to be zero to match the definition of integrated response. The corresponding bulk refractive index resolution of the 12 × 12 array is thus 7.3 × 10^{-6} RIU, *i.e.*, 0.015%/(2.05 × 10^3% per RIU). The peak wavelength shift under white light illumination corresponding to different bulk refractive indices is shown in Fig. S2.†

While integrating responses from all sensing elements promotes refractive index resolution, the spatial resolution is compromised. To determine the optimal balance between

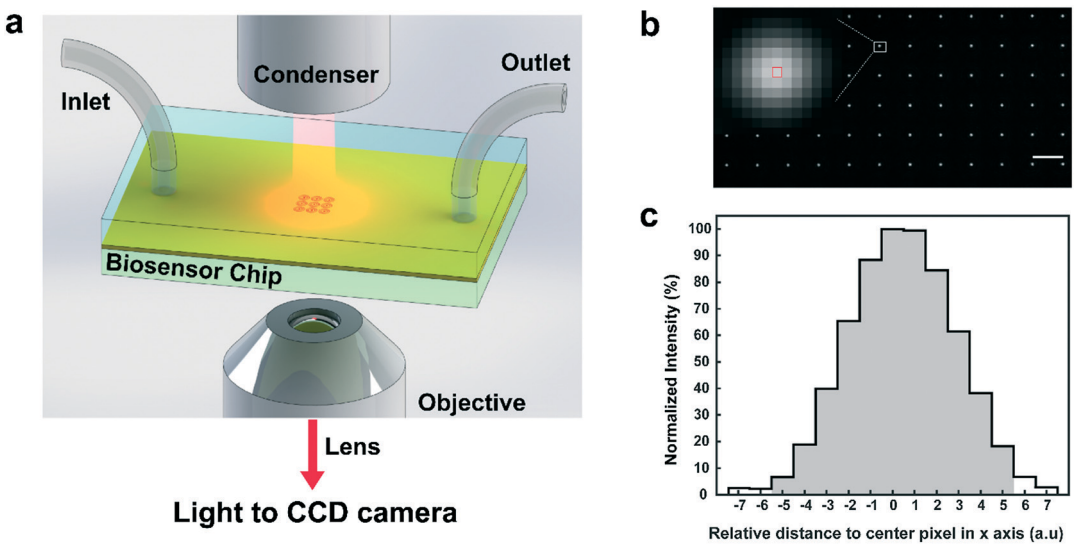

Fig. 2 Intensity-modulated detection scheme and optical images of the interferometer array. (a) Detection scheme of the nanoplasmonic interferometer. The biosensor is integrated with a microfluidic channel and is illuminated by collimated LED light through a condenser. The transmitted light is collected by a 40× microscope objective (NA = 0.6) and is coupled to a CCD camera *via* a focusing lens. (b) An optical transmission image of 12 × 6 array from the 12 × 12 sensor array. The inset is the zoomed-in optical image for a single sensing unit and the red dashed square labels the highest intensity pixel which represents the center of the sensor. Scale bar = 12.5 μm. (c) Relative intensity of neighbouring pixels relative to the center along the horizontal direction. The *X*-axis denotes the pixel distance from the center. Grey shaded areas denote the region over which the intensity integration is performed.

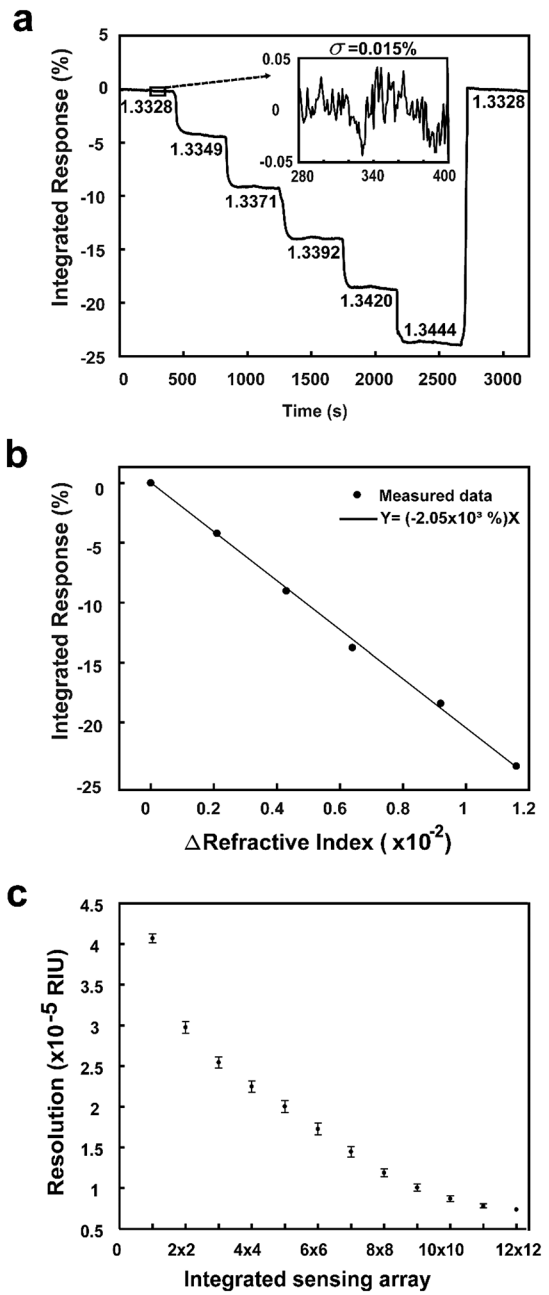

Fig. 3 Refractometric characterization of the interferometer. (a) Real-time response of the integrated 12 × 12 interferometer array in different glycerol–water concentrations. The inset shows a noise level of 0.015% over 2 minutes. (b) Relative intensity change in response to refractive index integrated over 12 × 12 interferometers. The dots are measured data and the line is a linear fitting. (c) Resolution as a function of integrated sensor number. The error bars represent standard errors.

both resolution requirements, we varied the number of sensing elements from which the signals were integrated. Responses from neighboring sensors were integrated as square matrices from 1 × 1 up to 12 × 12 elements. For comparison, the resolution of a single sensor response was also determined. It is found that the resolution improves by an order of magnitude from 4.1×10^{-5} to 7.3×10^{-6} RIU when the observation area increases from a single unit to the 12 × 12 array (Fig. 3c) and the corresponding footprint changes from $9.8 \times 9.8\ \mu m^2$ to $150 \times 150\ \mu m^2$. While the enhanced signal-to-noise ratio results from the larger number of sensors integrated, the footprint of the imaging pixel also increases, illustrating the tradeoff between the footprint and resolution. Depending on the application, the integration strategy could be selected to satisfy the specific need for spatial resolution and/or detection limit. It should be noted that, even with a single sensing unit, the measured resolution of 4.1×10^{-5} RIU is comparable to the performance of reported typical nanohole arrays,[38,39] but with a much smaller sensor footprint of only $9.8 \times 9.8\ \mu m^2$. Thus, the nanoplasmonic sensor presented here exceeds previously reported systems in combined performance, considering both spatial resolution and detection limit.

Detection of MMP-9 secreted from THP-1 cells

Following the characterization of the integrated response as a function of bulk refractive index by the intensity-interrogation mode, we applied the sensor to study biomolecular binding. Specific interactions between an antibody and antigen pair on the sensor surface increases the local refractive index. The corresponding sensor response can be used to monitor the amount of biomolecules in real-time without labeling. MMP-9 was selected as the target molecule in this study due to its important role in multiple physiological and pathological processes as mentioned before. It should be noted that although a single protein marker is detected in this work, the sensor array can be functionalized with different antibodies for multiplex sensing, since individual sensing elements are responsive to the local change of refractive index. The detection of cell culture supernatant, containing serum and other cell secretory molecules, represents a complex matrix that could potentially generates strong non-specific signals. To immobilize an antibody on the sensor, we established a surface modification protocol. As shown in Fig. 4a, the sensor was first soaked in MUA to form a self-assembled monolayer (SAM) containing a carboxyl tail (–COOH). Then the –COOH group was activated by soaking the sensor in EDC and NHS. The sensor was then assembled with a microfluidic channel and anti-MMP-9 was flowed in, resulting in immobilization of the antibody on the sensor surface. Glutaraldehyde was flowed in to lightly crosslink the antibody and prevent delamination,[40] followed by casein to block non-specific binding. The quality of surface modification was monitored by real-time tracking of the peak wavelength position in the wavelength-modulation mode (Fig. 4b). The modification was highly repeatable as shown in Fig. 4c, which is important for reproducible biomarker detection. In addition to demonstrating quality control, wavelength modulation was employed here to determine the optimal location of the red LED wavelength relative to the interference spectra, ensuring a unidirectional intensity shift upon subsequent MMP-9 binding.

To image the binding of antigen to the antibody-functionalized surface, the white light source was replaced by

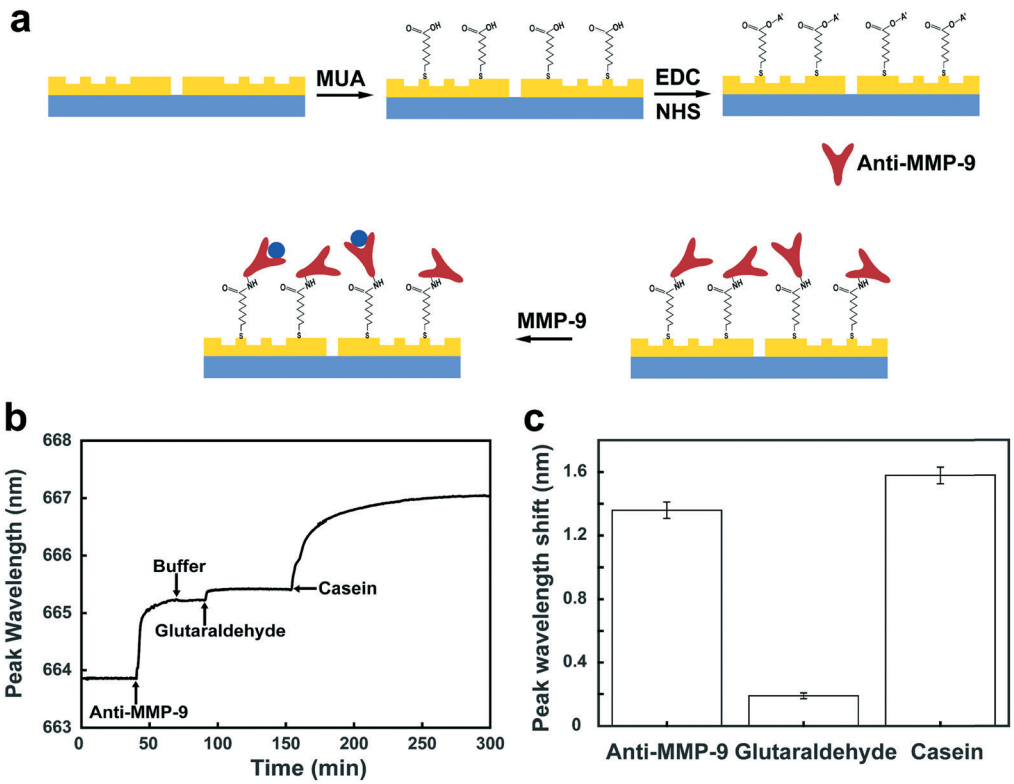

Fig. 4 Surface modification of the biosensor. (a) For MMP-9 detection, a self-assembled monolayer of MUA is formed on the gold surface, followed by activation of the carboxyl groups by EDC/NHS to crosslink anti-MMP-9. (b) Using the wavelength-modulation mode, the peak wavelength position was monitored for each surface modification step. (c) The peak wavelength shift in response to each surface modification step. The error bars denote the standard deviation from three independent experiments.

a monochromatic LED and the intensities transmitted by individual sensors were monitored. THP-1 culture medium was flowed in first to establish a stable baseline. Then various concentrations of MMP-9 in the culture medium (0, 50, 100, 150, 200 ng mL^{-1}) were flowed into the microfluidic chamber. The interaction time was fixed at 1.5 hour for each concentration. MMP-9 binding caused an increase in the refractive index above the sensor surface, resulting in a red shift of the interference spectra which decreases the transmitted intensity under ~661 nm single-wavelength illumination. The relative intensity change was normalized to the baseline (culture medium) for each sensing element. As shown in Fig. 5a, the 12 × 12 sensor array appears to respond immediately to MMP-9 binding upon exposure to a concentration of 50 ng mL^{-1}. The interaction during the first ~20 minutes interaction is relatively slow, as indicated by the gradual slope of the intensity response *versus* time in Fig. 5a between 30 and 50 minutes. This is due to MMP-9 capture and depletion upstream of the sensing area, resulting in a lower MMP-9 concentration above the sensors than the input concentration. As the upstream depletion gradually reduces with time, the sensor area is exposed to greater MMP-9 concentrations than during the first 20 minutes, leading to steeper intensity responses over time. As the culture medium contains 10% serum, the concentration of total proteins exceeds that of the target molecules by several orders of magnitude. Hence, the sensor response to addition of MMP-9 to the culture medium is not due to bulk refractive index change. Instead, it reflects specific surface binding, as culture medium alone generates a flat and stable response. Fig. 5b shows real-time integrated responses for various known MMP-9 concentrations, where stronger responses are observed for higher MMP-9 concentrations. Considering the surface area of 14 × 4 mm^2 and a monolayer of protein is a few ng mm^{-2}, the microfluidic channel must absorb at least 100 ng of MMP-9 to form a monolayer. This amount is comparable to the total MMP-9 injected into the microfluidic channel at the highest concentration of 200 ng mL^{-1}, and 100% protein capture may not be realistic especially considering continuous sample flow. Thus, the binding curves don't exhibit saturation due to the large capture area and insufficient MMP-9 injected into the device. Achieving saturation will require much longer sample injection especially at low MMP-9 concentrations. Although it would be ideal to flow the MMP-9 for longer periods to achieve surface saturation, the 1.5 hour sample flow is already a long assay and the sample concentration cannot be increased to accelerate surface saturation due to the intrinsic low concentration of MMP-9 in the supernatant. Fig. 5c demonstrates intensity responses recorded 90 minutes after MMP-9 injection which is where the greatest signal difference occurs for each of the known MMP-9 concentrations. The dots denote the average response from 144 sensing elements

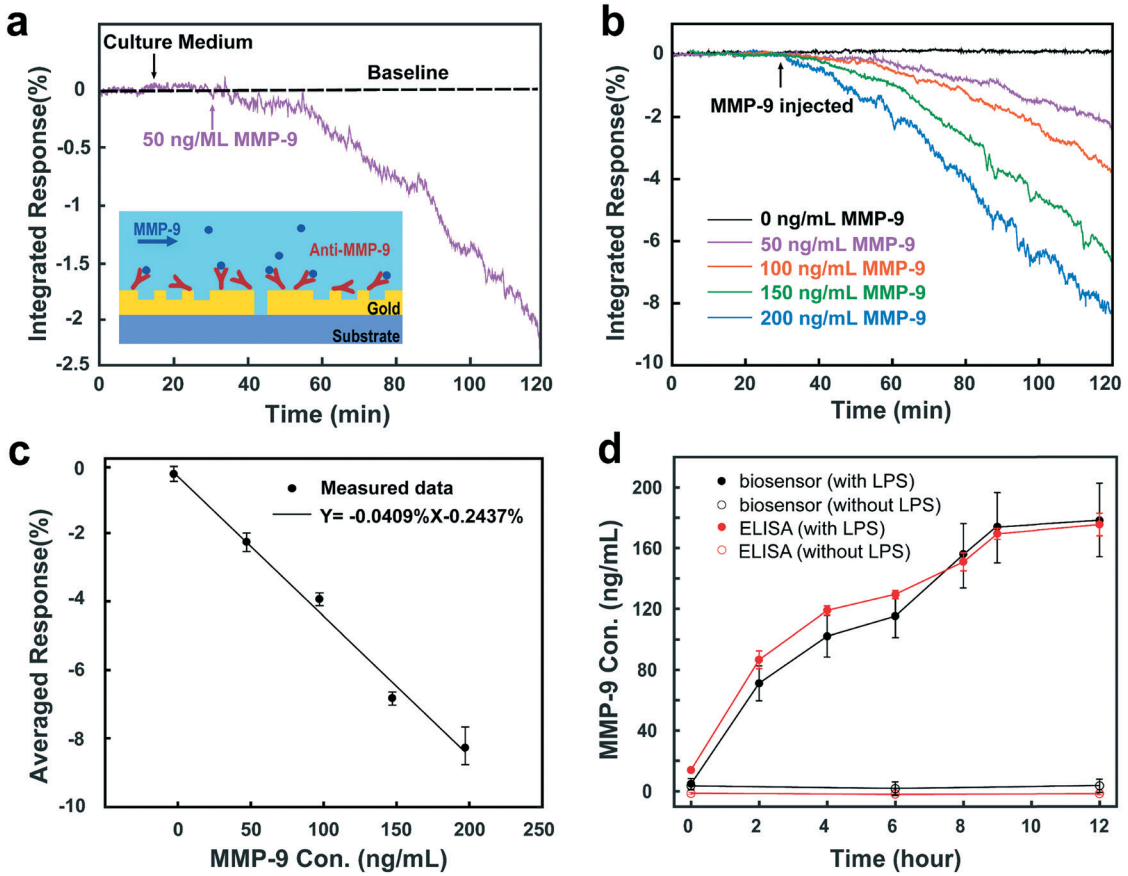

Fig. 5 MMP-9 detection results. (a) Real-time binding response of 50 ng mL^{-1} MMP-9 dissolved in culture medium (purple curve). The black dashed line is the baseline. The curve is integrated response of 144 sensing units. 50 ng mL^{-1} MMP-9 was flowed in after a stable baseline had been established with culture medium for ~30 minutes. (b) Real-time integrated responses from 144 sensing units for MMP-9 binding in different known concentrations. The arrow denotes the starting time point of MMP-9 injection. (c) The calibration curve obtained from solutions of known concentrations of MMP-9 ($n \geq 3$). (d) MMP-9 concentration detected in cell culture supernatant. The solid dots represent MMP-9 concentration from LPS stimulated cells detected by the plasmonic interferometric sensor (black) and ELISA (red), respectively; the open circles represent controls without LPS stimulation. The error bars denote the standard deviation among 144 individual sensing units for the plasmonic biosensor. The error bars in the ELISA results denote standard deviation from three independent repeats. Three independent repeats at 2nd, 4th and 8th hour timepoints have been performed with the plasmonic interferometer sensor and are shown in Fig. S4.†

and the error bars denote the standard deviation from three independent measurements. A linear relationship is observed between the intensity change and MMP-9 concentration. The linear regression model fitting for the MMP-9 calibration curve gives $R^2 > 0.98$. The signals are observed to be highly repeatable, and intensity change at a fixed hour correlates very well with concentration, even though saturation is not reached. The linear regression gives a response of 4.09% intensity change for every 100 ng mL^{-1} MMP-9 concentration and this calibration is applied for later MMP-9 detection in cell culture supernatant. The limit of detection (LOD), *i.e.*, the lowest concentration that the sensor can detect, is defined as three times the noise in the response of culture medium alone,[41] and it is calculated to be ≈17.8 ng mL^{-1}. Although not as sensitive as ELISA,[42] the nanoplasmonic sensor does not require labeling and is suitable for real-time analysis of cell response, which we will explore in our future work. It should be noted that, the affinity between antibody and antigen pair from different manufacturers may differ. Several products were tested and the pair with the best affinity, as determined by biosensing measurements, was chosen (Fig. S3†).

We next employed the calibration curve (Fig. 5c) to determine the amount of MMP-9 secreted from THP-1 cells as a function of time. To stimulate MMP-9 secretion, LPS was added to the culture medium containing the THP-1 cells, achieving a final concentration of 10 μg mL^{-1}.[43] Supernatant from the cells was extracted at selected time intervals and centrifuged before flowing into functionalized microchannels. The sensor response was measured using supernatant from cells stimulated up to twelve hours by LPS and the MMP-9 concentration was determined as a function of time as shown in Fig. 5d. The solid black dots denote the concentration detected from LPS stimulated cells and the open black circles are the response obtained from control samples where the supernatant was extracted in the same way except that the cells did not experience LPS stimulation. To test the device variability, three functionalized plasmonic

interferometer sensor arrays were used to test the same supernatant collected at 2nd, 4th and 8th hour time points each. Response from 144 sensing units in each array were integrated to represent the response from a single device, and the average and standard deviation from three independent devices were shown in Fig. S4.† The measurement was found to be highly repeatable among independent devices, and the device-to-device variability was less than the variability among sensing units in the same array. Encouraged by this high repeatability, supernatant from other time points was tested using a single array only. Fig. 5d captures the secretion dynamics of MMP-9 measured by the plasmonic sensor array up to twelve hours after LPS stimulation, and the error bars represent standard deviation of the 144 sensor responses from one array. Compared to bulk measurements in Fig. 3c, the variation of surface binding is relatively large. This could be a result of non-uniform MMP-9 binding on individual sensors in the array, due at least partially to antigen depletion from the bulk. It can be seen that the secreted MMP-9 concentration in the supernatant increases steadily with time, slowing around 8 hours and reaching a plateau around 9 hours. The total amount of MMP-9 secretion over an ~8 hour period is calculated to be $\sim 10^{-4}$ ng per cell based on the amount detected in the supernatant and known cell number. This value is comparable to findings in the literature.[34,44] In contrast, the supernatant from the control group without LPS stimulation generates minimal signals (open circles in Fig. 5d), demonstrating that the detected signal in the stimulation group represents specific binding of MMP-9.

To further validate the results from the nanoplasmonic biosensor, MMP-9 concentration in the supernatant was also assayed using a commercial ELISA kit (Fig. 5d). The concentration of MMP-9 *versus* stimulation time agrees well with that obtained from the plasmonic interferometer. As shown in Fig. S4,† the concentration also matched well with that detected from three independent measurements from the biosensor. This comparison demonstrates the reliability of our biosensor for quantitative biomarker analysis and underscores other notable advantages, including the capability for multiplex sensing in real-time, a small footprint, and lower assay time required.

While we demonstrate the detection of a single biomarker in this study, the measured temporal and spatial resolution *via* intensity modulation is suitable for multiplexed analysis. By creating different receptor arrays at different locations on the biosensor surface and integrating the cell culture with the microfluidic device, this interferometer platform will allow label-free, real-time detection of various analytes in complex biological fluids from small number of cells, an ongoing effort in our group.

Conclusions

In summary, we demonstrated that our nanoplasmonic interferometer, operated through intensity modulation, could provide both superior mass and spatial resolution for the study of immune-cell secretion in a label-free fashion. A high resolution of 4.1×10^{-5} RIU was demonstrated for single sensors with a footprint as small as 9.8×9.8 μm^2. By integrating responses from multiple sensing units, the resolution could be further improved to 7.3×10^{-6} RIU with a footprint of 150×150 μm^2. The biosensor reliably detected the concentration of biomarkers from a cell culture supernatant. The measured spatial and temporal resolutions are promising for multiplexed sensing in complex biological fluids.

Conflicts of interest

The authors don't have any conflict of interest to declare.

Acknowledgements

We wish to acknowledge the financial support from National Science Foundation (CBET-1512417).

References

1 J. Homola, *Chem. Rev.*, 2008, **108**, 462–493.
2 H. Raether, in *Surface Plasmons on Smooth and Rough Surfaces and on Gratings, Springer*, 1988, pp. 4–39.
3 S. A. Maier, *Plasmonics: fundamentals and applications*, Springer Science & Business Media, 2007.
4 E. Kretschmann and H. Raether, *Z. Naturforsch., A: Astrophys., Phys. Phys. Chem.*, 1968, **23**, 2135–2136.
5 J. Homola, S. S. Yee and G. Gauglitz, *Sens. Actuators, B*, 1999, **54**, 3–15.
6 D. Dorokhin, W. Haasnoot, M. C. R. Franssen, H. Zuilhof and M. W. F. Nielen, *Anal. Bioanal. Chem.*, 2011, **400**, 3005.
7 G. Spoto and M. Minunni, *J. Phys. Chem. Lett.*, 2012, **3**, 2682–2691.
8 B. Rothenhäusler and W. Knoll, *Nature*, 1988, **332**, 615.
9 C. L. Wong and M. Olivo, *Plasmonics*, 2014, **9**, 809–824.
10 C. T. Campbell and G. Kim, *Biomaterials*, 2007, **28**, 2380–2392.
11 J. S. Shumaker-Parry and C. T. Campbell, *Anal. Chem.*, 2004, **76**, 907–917.
12 N. C. Lindquist, A. Lesuffleur, H. Im and S.-H. Oh, *Lab Chip*, 2009, **9**, 382–387.
13 T. M. Chinowsky, T. Mactutis, E. Fu and P. Yager, *Smart Medical and Biomedical Sensor Technology*, 2004, vol. 5261, pp. 173–183.
14 K. A. Tetz, L. Pang and Y. Fainman, *Opt. Lett.*, 2006, **31**, 1528–1530.
15 J.-C. Yang, J. Ji, J. M. Hogle and D. N. Larson, *Biosens. Bioelectron.*, 2009, **24**, 2334–2338.
16 G. Lautner, J. Kaev, J. Reut, A. Öpik, J. Rappich, V. Syritski and R. E. Gyurcsányi, *Adv. Funct. Mater.*, 2011, **21**, 591–597.
17 G. Kim, L. Jiang, P. K. Rathod, C. T. Campbell, A. Nishimoto and V. Casasanta, *NSTI Nanotechnology Conference, 1*, 2005.
18 G. J. Nusz, S. M. Marinakos, A. C. Curry, A. Dahlin, F. Höök, A. Wax and A. Chilkoti, *Anal. Chem.*, 2008, **80**, 984–989.
19 B. Zeng, Y. Gao and F. J. Bartoli, *Appl. Phys. Lett.*, 2014, **105**, 161106.

20 X. Li, M. Soler, C. I. Ozdemir, A. Belushkin, F. Yesilkoy and H. Altug, *Lab Chip*, 2017, **17**, 2208–2217.
21 A. B. Dahlin, N. J. Wittenberg, F. Höök and S.-H. Oh, *Nanophotonics*, 2013, **2**, 83.
22 H. Im, J. N. Sutherland, J. A. Maynard and S.-H. Oh, *Anal. Chem.*, 2012, **84**, 1941–1947.
23 K.-L. Lee, P.-W. Chen, S.-H. Wu, J.-B. Huang, S.-Y. Yang and P.-K. Wei, *ACS Nano*, 2012, **6**, 2931–2939.
24 K. M. Mayer and J. H. Hafner, *Chem. Rev.*, 2011, **111**, 3828–3857.
25 T. W. Ebbesen, H. J. Lezec, H. F. Ghaemi, T. Thio and P. A. Wolff, *Nature*, 1998, **391**, 667.
26 C. Escobedo, *Lab Chip*, 2013, **13**, 2445–2463.
27 J. N. Anker, W. P. Hall, O. Lyandres, N. C. Shah, J. Zhao and R. P. Van Duyne, *Nat. Mater.*, 2008, **7**, 442.
28 Y. Gao, Z. Xin, B. Zeng, Q. Gan, X. Cheng and F. J. Bartoli, *Lab Chip*, 2013, **13**, 4755–4764.
29 M. P. McDonald, A. Gemeinhardt, K. König, M. Piliarik, S. Schaffer, S. Völkl, M. Aigner, A. Mackensen and V. Sandoghdar, *Nano Lett.*, 2018, **18**, 513–519.
30 W. C. Parks, C. L. Wilson and Y. S. López-Boado, *Nat. Rev. Immunol.*, 2004, **4**, 617.
31 A. Page-McCaw, A. J. Ewald and Z. Werb, *Nat. Rev. Mol. Cell Biol.*, 2007, **8**, 221.
32 J. Hu, P. E. Van den Steen, Q.-X. A. Sang and G. Opdenakker, *Nat. Rev. Drug Discovery*, 2007, **6**, 480.
33 B. Lelongt, G. Trugnan, G. Murphy and P. M. Ronco, *J. Cell Biol.*, 1997, **136**, 1363–1373.
34 S. H. Wu, K. L. Lee, A. Chiou, X. Cheng and P. K. Wei, *Small*, 2013, **9**, 3532–3540.
35 T. Thio, K. M. Pellerin, R. A. Linke, H. J. Lezec and T. W. Ebbesen, *Opt. Lett.*, 2001, **26**, 1972–1974.
36 G. Gay, O. Alloschery, B. V. de Lesegno, J. Weiner and H. J. Lezec, *Phys. Rev. Lett.*, 2006, **96**, 213901.
37 Y. Gao, Z. Xin, Q. Gan, X. Cheng and F. J. Bartoli, *Opt. Express*, 2013, **21**, 5859–5871.
38 H. Im, A. Lesuffleur, N. C. Lindquist and S.-H. Oh, *Anal. Chem.*, 2009, **81**, 2854–2859.
39 C. Escobedo, S. Vincent, A. I. K. Choudhury, J. Campbell, A. G. Brolo, D. Sinton and R. Gordon, *J. Micromech. Microeng.*, 2011, **21**, 115001.
40 I.-Y. Huang, C.-Y. Lin and E.-C. Wu, *J. Micro/Nanolithogr., MEMS, MOEMS*, 2010, **9**, 023008.
41 D. MacDougall and W. B. Crummett, *et al.*, *Anal. Chem.*, 1980, **52**, 2242–2249.
42 D. Leppert, S. L. Leib, C. Grygar, K. M. Miller, U. B. Schaad and G. A. Holländer, *Clin. Infect. Dis.*, 2000, **31**, 80–84.
43 H. Valleala, R. Hanemaaijer, J. Mandelin, A. Salminen, O. Teronen, J. Mönkkönen and Y. T. Konttinen, *Life Sci.*, 2003, **73**, 2413–2420.
44 B. Wong, W. C. Lumma, A. M. Smith, J. T. Sisko, S. D. Wright and T. Q. Cai, *J. Leukocyte Biol.*, 2001, **69**, 959–962.

